Nanostructured carbons modified with nickel as potential novel reversible hydrogen storage materials: Effects of nickel particle size

P.M. Carraro[a,b], A.A. García Blanco[c], G. Lener[d], D. Barrera[c], S. Amaya-Roncancio[c], C. Chanquía[e], H. Troiani[e], M.I. Oliva[b], G.A. Eimer[a,*]

[a] *CITeQ – CONICET – UTN, Maestro López y Cruz Roja Argentina, Ciudad Universitaria, 5016, Córdoba, Argentina*
[b] *IFEG – CONICET – UNC, Medina Allende, Ciudad Universitaria, 5016, Córdoba, Argentina*
[c] *INFAP – CONICET – UNSL, Ejército de los Andes 950, 5700, San Luis, Argentina*
[d] *INFIQC – CONICET – UNC, Ciudad Universitaria, 5016, Córdoba, Argentina*
[e] *CAB – CNEA, Bustillo, 9500, San Carlos de Bariloche, Río Negro, Argentina*

ARTICLE INFO

ABSTRACT

In this study, ordered mesoporous carbons CMK-3 were prepared by a nanocasting method using SBA-15 silica as template and sucrose as carbon source. The pure CMK-3 was modified with nickel by wet impregnation method and the effects on hydrogen storage capacity were studied at different pressures and temperatures. The structural, textural and chemical properties were evaluated in order to investigate their correlation with hydrogen adsorption properties. Also, computational methods (DFT) contributed to the understanding of hydrogen storage interactions in the Ni/C samples.

Two different behaviors on the hydrogen adsorption were obtained after reduction treatment under H_2 atmosphere. For the unreduced samples at 77 K, the textural properties were the determining factor in the H_2 storage capacity. On the other hand, for the reduced samples at room temperatures, the presence of nickel nanoparticles increased the hydrogen adsorption, with a possible dependence of the particle size.

1. Introduction

Since the 1970s, hydrogen has been considered as an attractive energy carrier for the storage of renewable energy [1]. The physical and chemical properties of hydrogen are in many cases unique despite the fact that hydrogen appears to be the simplest element. For on-board use, the issue is the amount of hydrogen that can be safely stored in a vehicle and delivered as required under operational conditions. In addition, hydrogen storage must be reversible at or near room temperature. Thus, the major scientific challenge is to design low-cost, lightweight materials that can reversibly and rapidly store hydrogen near ambient conditions at a density equal to or greater than liquid hydrogen [2]. An interesting alternative is the physisorption, which provides fast adsorption/desorption kinetics and almost instantaneous equilibrium between adsorbed hydrogen and hydrogen in the gas phase. Thus, materials with large surface areas and low densities, such as nanostructured carbons, are attractive for hydrogen storage applications, which is the main bottleneck for the realization of on-board hydrogen fuel cell vehicles. In the last years, numerous synthesis methods have been studied for obtaining porous carbon materials with interesting textural properties. Among them, carbons mesostructured from Korea (CMK) have gained important attention. The high control of the specific surface, significant flexibility in the pore size and structural diversity of ordered mesoporous carbonaceous materials, make them good candidates for diverse applications [3,4]. Moreover, the metal incorporation into carbon materials promotes the presence of active sites, contributing to improve hydrogen storage [5]. The use of noble metals is often economically non-viable. Therefore, recent studies have been geared towards substituting noble with transition metals. Thus, promising results were obtained by means of "spillover" effect by employing various carbon, zeolites, MOFs materials, doped with Pt, Ni, Pd, Ru [5]. Spillover of atomic hydrogen is a well-documented mechanism in heterogeneous catalysis [6,7] however, the details of spillover based hydrogen storage processes have not yet been well understood since it is difficult to obtain direct evidence of the mechanism [8].

Another possible route for improving the hydrogen storage is via Kubas-type interaction [9], due to empty d-orbitals of transition metal centers [10]. The Kubas interaction strength stands midway between hydrides and physisorption in binding strength. Thus, Anbia et al. [11] have studied the effect of mesoporous carbon CMK-3 as support on Pt

catalytic activities, dissociation of hydrogen molecules and enhanced hydrogen absorption on modified MIL-101 (MIL, Matérial Institut Lavoisier) at room temperature. At the same time, Giasafaki et al. [5] have presented a significant enhancement of the hydrogen storage capacity upon (Pd) metal-doping at room temperature. Meanwhile, Huang et al. [12] have found that cobalt-embedded ordered mesoporous carbon (OMC) materials present higher hydrogen adsorption capacity than the OMC pure, due to the Kubas-type interaction between Co and H_2. Also, the hydrogen spillover effect might occur in parallel. Among transition metals for enhancing hydrogen storage capacity, nickel is particularly promising because it is abundant, inexpensive compared to other metals, and is able to enhance hydrogen storage properties. Juárez et al. [13] studied the introduction of Ni into CMK-1, displaying improved results in hydrogen at 77 K and high pressure (10 bars) that at low pressure.

Despite the different properties of these materials that can influence the storage capacity, like specific area, composition and pore size, it is necessary to understand the mechanism of hydrogen uptake to improve these materials for hydrogen storage. Several authors have attributed to the enhance of hydrogen storage capacity of different carbon materials to a spillover effect. However, spillover effect remains controversial, and understanding and more information about this phenomenon are still needed [14].

Thereby, in previous reports [15], we have shown the hydrogen adsorption behavior at 77 K and ambient temperature of Ni/SiO_2 system indicated a different mechanism of sorption at those temperatures. In addition, Density Functional Theory (DFT) calculations showed that the spillover effect was energetically unfavorable. Thus, we considered a possible hydride formation at room temperature.

In this sense, this work aims to examine hydrogen storage capacity of ordered mesoporous carbon CMK-3 modified with nickel. The textural and chemical properties were evaluated and discussed regarding the hydrogen adsorption. Based on DFT calculations, the focus of the work is to find key factors in hydrogen storage to understand the H_2 adsorption mechanism and direct the design of carbon-based hydrogen adsorbents systems.

2. Material and methods

2.1. Synthesis of mesoporous carbon

The synthesis of the ordered mesoporous carbon CMK-3 was carried out using SBA-15 silica as template and sucrose as carbon source, following the synthesis procedure described by Barrera et al. [16]. The synthesis procedure of ordered mesoporous silica SBA-15 is reported by Carraro et al. [17].

The CMK-3 was synthesized via a two-step impregnation of the mesoporous SBA-15, with a solution of sucrose dissolved in sulfuric acid and water in a mass ratio of 1:1.3:0.14:5 (SBA-15:Sucrose:H_2SO_4:H_2O). The mixture was stirred at room temperature for 1 h and then it was dried at 373 K for 6 h and subsequently at 433 K for 6 h. A second impregnation with a mixture of sucrose aqueous solution, sulfuric acid and water with a mass ratio of 0.8:0.09:5 was performed to ensure the template pore filling. This mixture was treated again at the same drying conditions to complete the polymerization step. Then, the resultant dark brown colored composite was heated from room temperature (RT) up to 1173 K for 6 h under a N_2 flow of 180 mL/min with a heating rate of 3 K/min to complete carbonization.

The silica template was dissolved in a 5 wt.% hydrofluoric acid solution at RT for 24 h. The template-free carbon obtained was filtered, washed with deionized water and ethanol (50:50% v/v) until the conductivity value was smaller than 10 μS/cm. Finally, the nanostructured carbon was dried overnight at 353 K.

2.2. Synthesis of Ni/CMK-3 mesoporous carbon

The ordered mesoporous carbon CMK-3 was modified with Ni by wet impregnation method using nickel nitrate (Ni(NO$_3$)$_2$·6H$_2$O, Merck) as the source of nickel. The mesoporous carbon CMK-3 was mixed with a solution of Ni(NO$_3$)$_2$·6H$_2$O in ethanol with a concentration corresponding to the desired metallic loading (2.5 and 10 wt.%) and a rotary evaporator was used to remove excess of ethanol at about 323 K. The solution was held in a flask, which was partially submerged in the water bath, and powered by a motor which slowly rotates the flask for an even heat distribution. The impregnated samples were dried at 333 K overnight and were thermally treated in a N_2 flow (25 mL/min) at 473 K for 5 h. Subsequently, the temperature was increased to 773 K with a heating rate of 4 K/min and kept during 5 more hours. The synthesized samples are denoted as Ni/CMK-3(x), where x indicates the expected metal loading percentage (nominal loading).

2.3. Characterization

The textural characterization was carried out by N_2 adsorption-desorption isotherms at 77 K (N_2 with 99.999% purity) in an ASAP 2000 equipment (Micromeritics Instrument Corporation, USA). Adsorption isotherms were acquired in a scale of relative pressures of p/p_0: from 0.001 to about 0.985 (adsorption branch) and from 0.985 to 0.3 (desorption branch). The total number of adsorption/desorption data points was 105 (adsorption: 68 and desorption 37). Free-space calibration using He and the interval equilibrium time was 25 s. Before the measurements, the samples were degassed at 523 K for 12 h under vacuum. The specific surface area (S_{BET}) was calculated by the Brunauer-Emmett-Teller (BET) method using the adsorption data, in the pressure range of p/p_0: 0.05–0.25, where the conditions of linearity and considerations regarding the method were fulfilled. The total pore volume (V_{TP}) was calculated at a relative pressure of 0.98 [18], and the micropore volume ($V_{\mu P}$) and primary mesopore volume (V_{MP}) were calculated by αS-plot method using the standard isotherm GCB-1. The pore size distributions of the samples were determined by *QSDFT* method (Quenched Solid State Functional Theory) using the Quantachrome software, with the kernel N_2 at 77 K on carbon, slit/cylindrical pores, adsorption branch.

The samples were also analyzed by X-ray diffraction (XRD) using a PANanalytical Empyrean diffractometer with Cu Kα radiation (λ = 1.5418 Å) in the range of *2θ* from 0.7 to 7° and from 10 to 80°. The scan step was 0.05° with a step time of 8 s for the analysis.

Transmission electron microscopy (TEM) images were collected using a Philips CM200UT transmission electron microscope. Samples were dispersed in ethyl alcohol 99.5% and a drop of the suspension was deposited on a lacey carbon copper grid.

Scanning electron microscopy (SEM) images of the materials were obtained on a SEM-FEG Nova NANO-SEM 230. Gold coverage was applied to make samples conductive. The acceleration voltage was 20 kV.

Fourier Transform Infrared Spectroscopy (FTIR) was measured in a System 2000–Perkin Elmer spectrometer in an optical range of 400–3000 cm^{-1} at a resolution of 4 cm^{-1}.

Temperature-Programmed Reduction (TPR) was performed on a ChemiSorb 2720 apparatus (Micromeritics Instrument Corporation, USA), in a temperature range from room temperature to 1073 K with a heating rate of 10 K/min in a binary gas flow (5 vol % H_2/N_2) of 20 mL/min STP, and the reduction reaction was monitored by the H_2 consumption with a thermal conductivity detector (TCD).

X-ray photoelectron spectra (XPS) were obtained in a VG Microtech ESCA apparatus equipped with an Al anode (Al Kα radiation, 1486.6 eV) and VG100AX spherical analyzer.

Hydrogen adsorption measurements at 77 K and pressures up to 10 bar were performed in a static volumetric system (Micromeritics Instrument Corporation, USA, ASAP, 2050), appropriately calibrated. High-pressure adsorption isotherms of hydrogen were measured at

293 K in a high-pressure manometric system HPA 100 (VTI Corporation). For the adsorption experiments, high-purity hydrogen gas (99.999%) was used. Previous to adsorption experiments, samples were degassed at 573 K during 12 h under vacuum conditions $(5 \times 10^{-3}$ mmHg). Before each analysis, helium was used to measure the void volume of the sample cell in both instruments.

2.4. Computational methods

DFT calculations were performed using the Quantum Espresso package [19]. The generalized gradient approximation (GGA) functional Perdew–Burke–Ernzerhof (PBE) was used [20]. Ultra-soft pseudopotentials with scalar relativistic correction generated by Rappe-Rabe-Kaxiras-Joannopoulos method (RRKJUS) were employed to describe the electron-ion interaction [21]. The chosen energy cutoff was 40 R y and the threshold for self-consistency of 1×10^{-5} eV. Brillouin zone integration was approximated using the Monkhorst–Pack scheme with $3 \times 3 \times 1$ k-point sampling [22]. Graphene calculations were performed with a (3×3) supercell with 11 Å vacuum. All atoms of the Ni/graphene model were free to relax to find minimum energy position of all involved atoms [23]. The geometry relaxation was done using BFGS quasi-Newton algorithm until the forces on each atom were less than 10^{-5} eV/Å and the energy difference of consecutive steps was less than 10^{-5} eV. The study of the minimum energy paths was undertaken using the nudged elastic band method (NEB) [24], and local minimum were found through the conjugate gradient CG technique. All the molecular and density plots were made with the XCrySDen package [25].

3. Results and discussion

3.1. Textural and physico-chemical characterization

The well-ordered mesoporous structure of the materials was confirmed by N_2 sorption measurements at 77 K. Fig. 1. a shows the experimental nitrogen adsorption–desorption isotherms of the CMK-3 and Ni/CMK-3 materials, and the SBA-15 isotherm is shown in the inset. According to the IUPAC classification [26], the isotherms of both materials are Type IV characteristics of mesoporous structures. The sharp inflection in the adsorption branch at $p/p^0 \sim 0.5$ and the close hysteresis at $p/p^0 \sim 0.4$ indicate a well-ordered mesoestructure with limited restrictions to the pore. The similar shape of the CMK-3 and the Ni/CMK-3 materials suggests that the ordered mesoporous structure has been kept after nickel impregnation.

The SBA-15 sample presents Type H1 hysteresis loop, associated with capillary condensation and desorption in open-ended cylindrical mesopores, which is typical of materials with cylindrical geometries and uniform pore size [17,27]. On the other hand, the hysteresis loop of the mesoporous carbon materials exhibits some Type H2 characteristics, where the desorption branch is slightly more pronounced than the adsorption branch [16]. This behavior could be due to the pore blocking affecting the pressure of evaporation/desorption in the pore. Thus, the pore size distribution (PSD) curves must be obtained from the adsorption branch. Fig. 1. b shows the pore size distribution curves. These materials exhibit a similarly narrow and a bimodal pore size distribution, with micropores sizes around 0.8 nm and mesopores sizes in the range of 3–6 nm, centered at 4.7 nm pores.

The textural properties are shown in Table 1. All the samples present high specific surface and pore volume, showing a decrease of these values with the increasing of Ni loading (Ni/CMK-3 (10)). According to our previous studies [17,28], metal loading into the mesoporous structures would lead to loss in the hexagonal pore arrangement. However, it is worth noting for Ni/CMK-3 (2.5) sample that both the isotherm and the PSD are not affected by impregnation with nickel, since they are very similar to the pure carbon CMK-3, suggesting a good dispersion of Ni nanoparticles in the mesoporous carbon.

Fig. 2. a shows the low-angle XRD patterns of CMK-3 and Ni/CMK-3

samples. The CMK-3 material exhibits three well-resolved peaks that can be indexed as the spaces of (100), (110), and (200) planes, consistent with the 2-D hexagonal symmetry (p6mm) derived from the structural order of the solid SBA-15 (figure inset) [3]. The reflection intensity of the main peak (100) is got weakened and broadened, and the (110) and (200) peaks disappeared with the nickel loading increasing, indicating some loss of structural order [29]. However, the diffractograms for all samples suggest that these materials present ordered mesoporous structure with hexagonal pore array, characteristics of these kinds of mesoporous carbon materials [3,16,30].

On the other hand, high angle X-ray diffraction measurements were performed on the CMK-3 and Ni/CMK-3 carbon materials, to identify the corresponding peaks of graphite structure and nickel species formed on the support (Fig. 2.b). As expected, for CMK-3 the two broad diffraction peaks at 23° and 43° corresponding to (002) and (100) planes are observed, which are characteristics of the graphite structure. Also, the XRD patterns of the Ni/CMK-3 samples exhibited similar diffraction peak positions, indicating that similar phases were dispersed on the surface support. Ni/CMK-3 (10) sample shows the graphite peak $(2\theta = 23°)$ and three narrow and intense peaks at $2\theta = 44.4, 51.7$ and 76.5°, assigned to nickel carbide (NiC) phase (JCPDS N° 45-0979). The Ni/CMK-3 (2.5) sample presents only hints of the mentioned peaks. Moreover, no peaks corresponding to nickel oxide were observed. This fact suggests that the oxides, if any, are clusters or particles too small to be detected by XRD (< 4–6 nm).

Previous results [31,32] showed that nickel carbide can be formed under an inert atmosphere at a temperature about 773 K. In addition, it is noteworthy that the Ni metal phase peak appears near the NiC signal, which may be overlapping. Many others works have suggested the presence of metallic nickel in carbon framework during thermal treatment (up to 773 K) in H_2 atmosphere absence, due to the reducing nature of the carbon [30,33]. However, Nagakura et al. [34] have reported that the carbide decomposition to nickel and carbon is carried out at very high temperatures, and Cao et al. [35] suggested that the carbon framework might reduce the surface energy of NiO, which would passivate and stabilize the NiO nanoparticles. Therefore, we could discard the metallic Ni presence on the mesoporous carbon, due to the calcination temperature employed.

Fig. 3 shows TEM images of the SBA-15 template (a-b) and the CMK-3 nanostructured carbon (c-d). Fig. 3. c corresponds to the frontal view to the direction of the hexagonal arrangement of unidirectional mesopores. The average pore size is about 5 nm, which is close to that obtained from N_2 adsorption–desorption isotherms. Fig. 3. d shows the perpendicular view to the direction of the pore arrangement. The images of CMK-3 exhibit well-ordered parallel straight mesochannels, similar to the SBA-15 template. In addition, as shown in Fig. 4.a-b, the Ni/CMK-3 (2.5) sample presents a long-range ordered mesostructure, characteristic of the CMK-3 materials, even after the Ni loading [36]. Moreover, it can be found darker spots in the TEM images, uniformly dispersed, that randomly interrupt the pore arrangement characteristic of the mesoporous materials, which can be attributed to the presence of nickel species over the CMK-3 framework [37,38]. The diameters of these nanoparticles were about 4–10 nm, which is indicative that some nickel species could be located inside the mesoporous channels.

Fig. 5 presents the TEM images of the Ni/CMK-3 (10) sample, where is showed that the mesoporous structure has been well preserved. In addition, it could be observed high-contrast regions, corresponding to nickel particles finely dispersed inside the channels as well as large particles on the external surface, whose size of these species is around 10 nm, aggregated into larger secondary particles [39]. Fig. 5. c shows the magnification of the marked region, where some small particles of nickel are observed, filling the interior of the channels.

The TPR curves for the Ni/CMK-3 samples are presented in Fig. 6. The Ni/CMK-3 (10) sample shows two reduction peaks at a different temperature, which are related to the different interaction with the support and locations of Ni. A first peak appears about 500 K, which
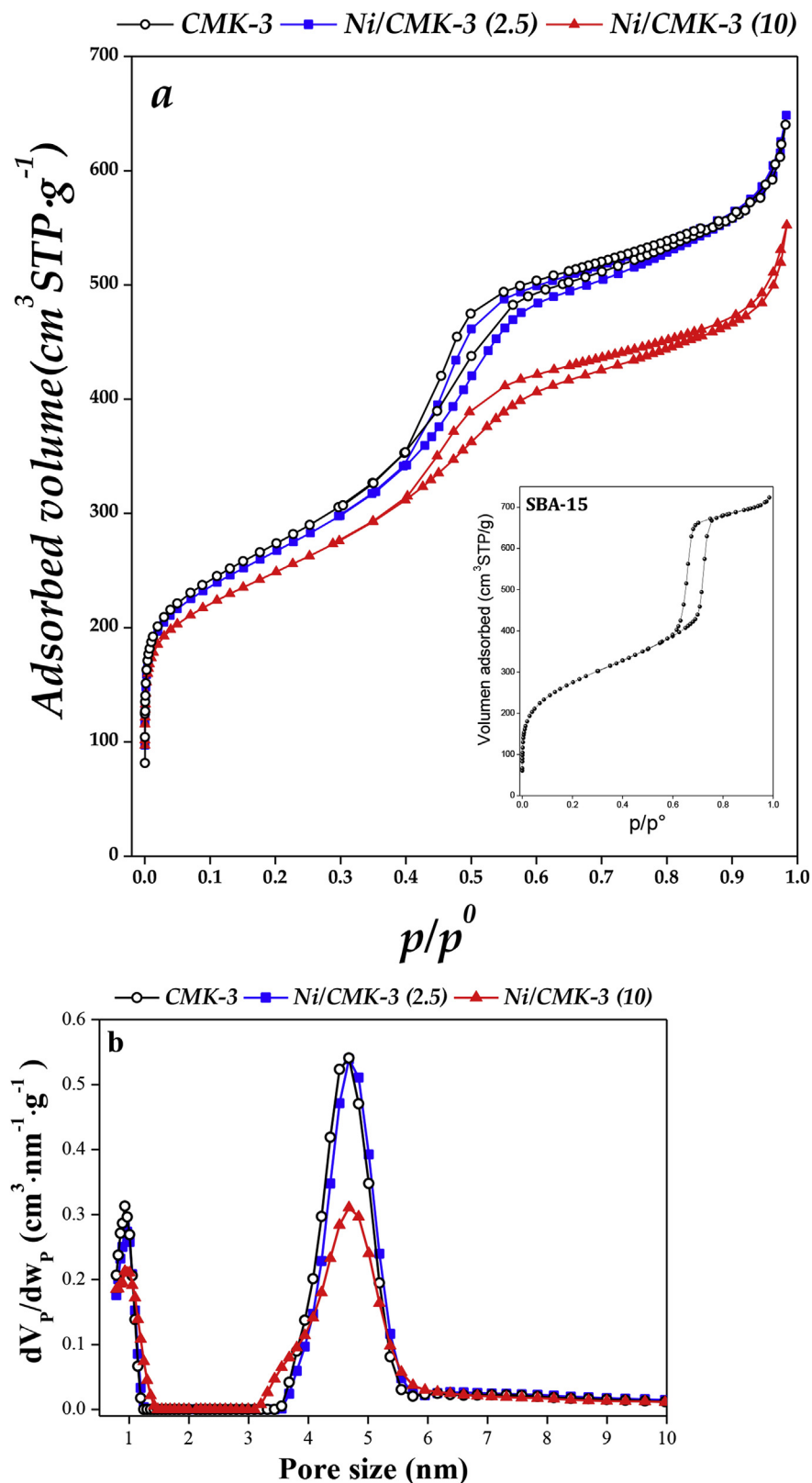
Fig. 1. (A) N_2 adsorption–desorption isotherm at 77 K (SBA-15 isotherm is shown inset) and (b) pore size distribution of the samples.

could be ascribed to Ni species dispersed on the surface and weakly interacting with the framework, probably nickel carbide, as it is suggested by previous results [32]. On the other hand, the second peak at 780 K, which can be mainly, attributed to the reduction of Ni species located inside the carbon framework and strongly interacting with the

support. These species could be NiO, due to the higher reduction temperature, or a possible coexistence of both phases. These peaks are less intense in Ni/CMK-3 (2.5) than Ni/CMK-3 (10) sample.

XPS spectra of the samples were measured to characterize the surface properties. Fig. 7 shows the spectra of the C 1s and Ni 2p signals of

Table 1
Textural properties of SBA-15, CMK-3 and Ni/CMK-3 materials.

Sample	S_{BET} $(m^2g^{-1})^a$	V_{TP} (cm^3g^{-1})	V_{MP} $(cm^3g^{-1})^b$	$V_{\mu P}$ $(cm^3g^{-1})^b$
SBA-15	992	1.20	0.80	0.06
CMK-3	972	0.99	0.43	0.16
Ni/CMK-3 (2.5)	948	0.99	0.40	0.16
Ni/CMK-3 (10)	884	0.84	0.31	0.16

[a] Determined by BET.
[b] Primary mesopores volume (V_{MP}) and micropores volume ($V_{\mu P}$) determined by αS-plot method.

Ni/CMK-3 (2.5) and Ni/CMK-3 (10) samples. The C 1s peak shows the characteristic shape of carbon materials, with the highest contribution at binding energy at ~ 284.0 eV, attributed to the sp² C=C and sp³ C-C carbon [40]. The C 1s signal was deconvoluted into contributions from 284.3 eV (assigned to sp² and sp³ of C=C and C-C, 64.6% in Ni/CMK-3 (2.5) and 65.58% in Ni/CMK-3 (10)), 285.3 eV (assigned to C-OH, 20.1% in Ni/CMK-3 (2.5) and 16.3% in Ni/CMK-3 (10)), 287.3 eV (assigned to C=O, 6.6% in Ni/CMK-3 (2.5) and 9.2% in Ni/CMK-3 (10)), and 290.1 eV (assigned to COOH, 8.7% in Ni/CMK-3 (2.5) and 8.8% in Ni/CMK-3 (10)). The assignment of the binding energies was performed according to [41]. The results show the main contribution from C-C and C=C carbon, due to the nature of CMK-3 materials, but also contributions from oxygen functional groups present in the samples.

Ni 2p signal is shown for the Ni/CMK-3 (2.5) and Ni/CMK-3 (10) samples. The signal of the Ni/CMK-3 (2.5) sample is remarkably low, due to the low metal loading, but also could be an indication of the location of the element at the interior of the porous material. The low intensity signal observed has a main contribution around 854.5 eV, which corresponds to the binding energy of Ni 2p$_{3/2}$ in its Ni²⁺ oxidation state (NiO) [42]. The Ni/CMK-3 (10) sample shows a characteristic signal of Ni²⁺, with a peak signal of 2p$_{3/2}$ at 854.5 eV, a satellite peak at ~ 861 eV, and a spin-orbit splitting of 18.5 eV between the Ni 2p$_{3/2}$ and 2p$_{1/2}$, that corresponds to the one reported for NiO. However, a signal is observed around 851.8 eV, which could be assigned to the presence of nickel carbide [43], in accordance with the XRD data. Therefore, it is considered possible the coexistence of both phases in the material.

3.2. DFT calculations

3.2.1. Hydrogen adsorption on nickel/carbon system

DFT calculations were performed to characterize the electronic interaction between supported nickel/carbon and hydrogen. The carbon was modeled as a graphene sheet. The model consisted of a Ni atom positioned on the Hollow site of a 3 × 3 graphene cell with a slab vacuum distance of 11 Å. All the calculations were implemented with dispersion correction to take into account long range interactions as described in Ref. [44]. The bonding energy of Ni atom on graphene was calculated to be −1.51 eV.

H₂ adsorption was studied with an initial state of a H₂ molecule at a distance of 0.74 nm from the Ni/C surface, and the final state considered was two individual H atoms bonded to the Ni atom at 0.155 nm (See Figure S2 – Supporting information). The study of the minimum energy path was undertaken using the nudged elastic band method (NEB), which showed that H₂ adsorption on graphene-supported Ni is a non-activated process with a reverse barrier of 1.35 eV, indicating the spontaneity of H₂ chemisorption on Ni (See Figure S3 – Supporting information). In comparison with the H₂ on clean graphene, the adsorption energy is increased, from −0.060 eV to −1.35 eV. The adsorption of H₂ on graphene-supported Ni is in accordance with Sigal
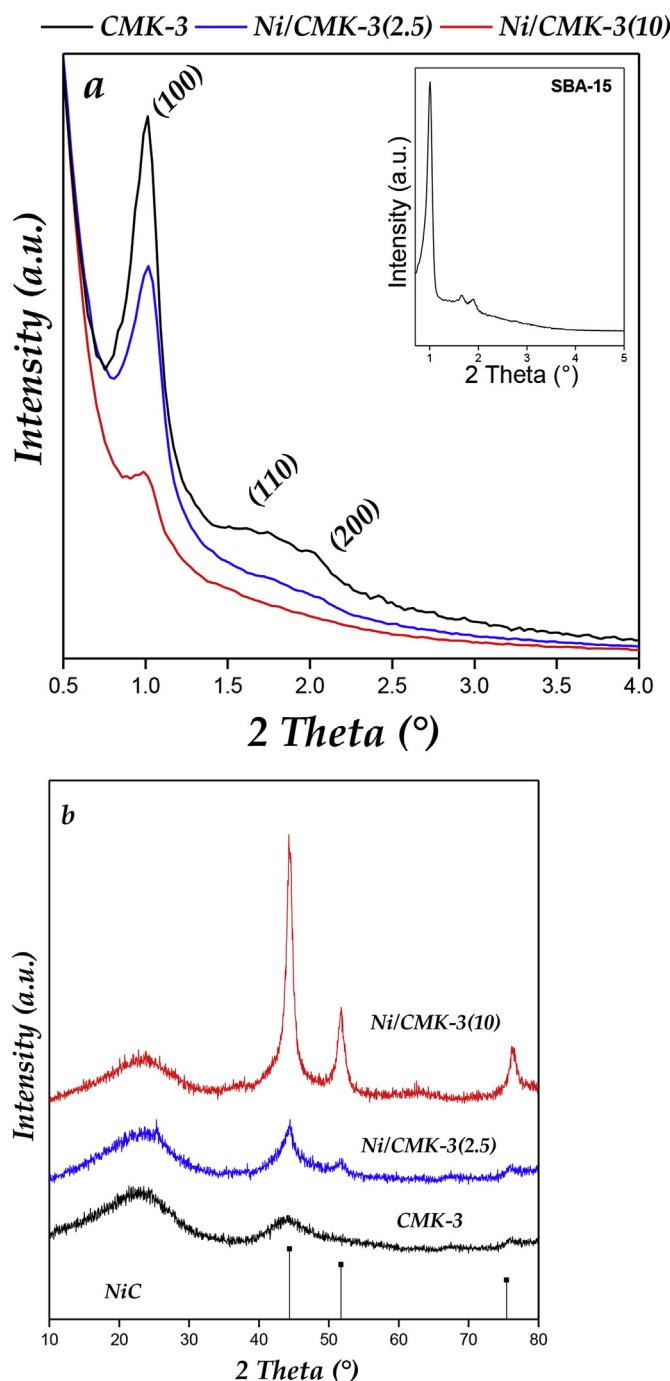
Fig. 2. (A) Low-angle XRD patterns of nanostructured carbons and SBA-15 (inset) and (b) high-angle XRD patterns of CMK-3.

et al. [45] who found a value of −1.21 to H₂ adsorbed on Ni bonded in Hollow site of graphene.

Differential density of charge was calculated to understand the electronic nature of the bonding in the present systems (Fig. 8). It is possible to appreciate accumulation lobes around the Ni-Carbon interaction and a high accumulation of electron charge around hydrogen bonded to Ni. The present fact in conjunction with calculated adsorption energy and DOS calculations (Fig. 9), indicates a covalent nature of involved H-Ni atoms. Thus, Fig. 9 shows the electronic density of states projected to the atoms involved in the H₂/Ni/graphene interaction. An overlap of states over the nickel and hydrogen molecule near of the Fermi level is observed. This indicates that the effective electronic overlap between these electronic states could form a strong interaction
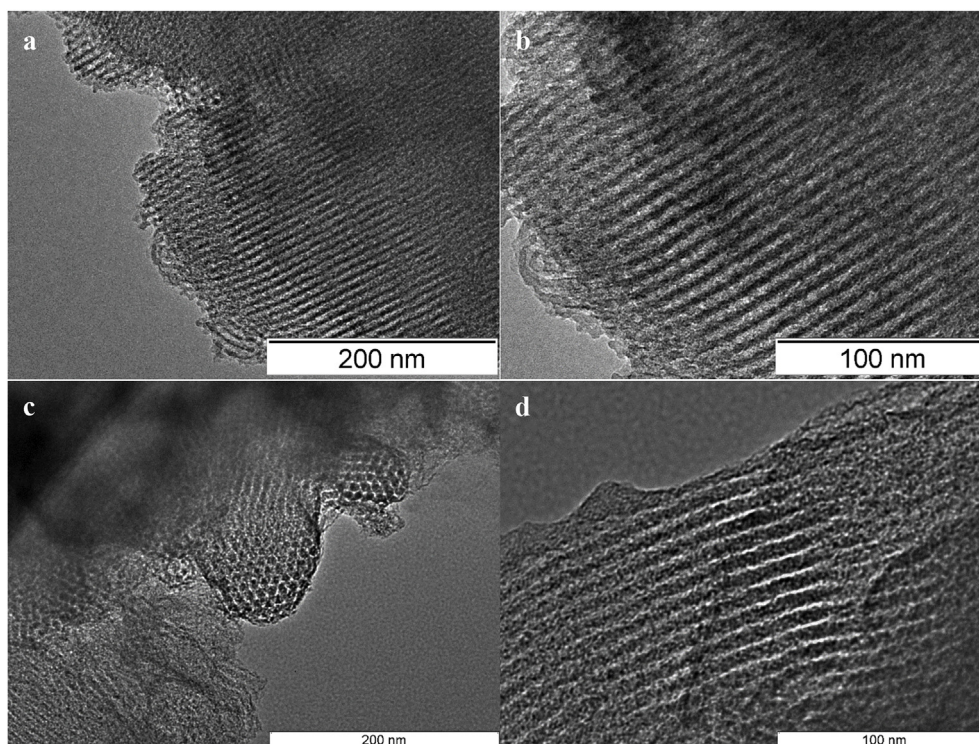
Fig. 3. Transmission electron microscopy images of (a–b) SBA-15 and (c–d) CMK-3.

and gives an effective bond. On the other hand, the interaction of the electronic state of the C bonded to Ni is observed about $-3\,eV$ under the Fermi level.

3.2.2. Hydrogen adsorption on Ni-C/carbon system

In order to deepen in the behavior of the H_2 adsorption at 77 K of the samples without reduction treatment, DFT calculations were performed considering Ni-C anchored on the graphene surface as a possible adsorbent material. The projected density of states plots of the NiC/graphene system showed an effective overlap between the electronic states of the Ni (See Figure S4 – Supporting information). Two geometries of the H_2 molecule interacting with the Ni-C group were considered (See Figure S5. a – Supporting information). First, the H_2 molecule was placed onto the Ni-C structure. The optimized geometry 1 shows that the H_2 molecule moves away from the Ni-C indicating that the interaction Ni-C-H_2 is not favorable (Fig. S5.a-b). In the second
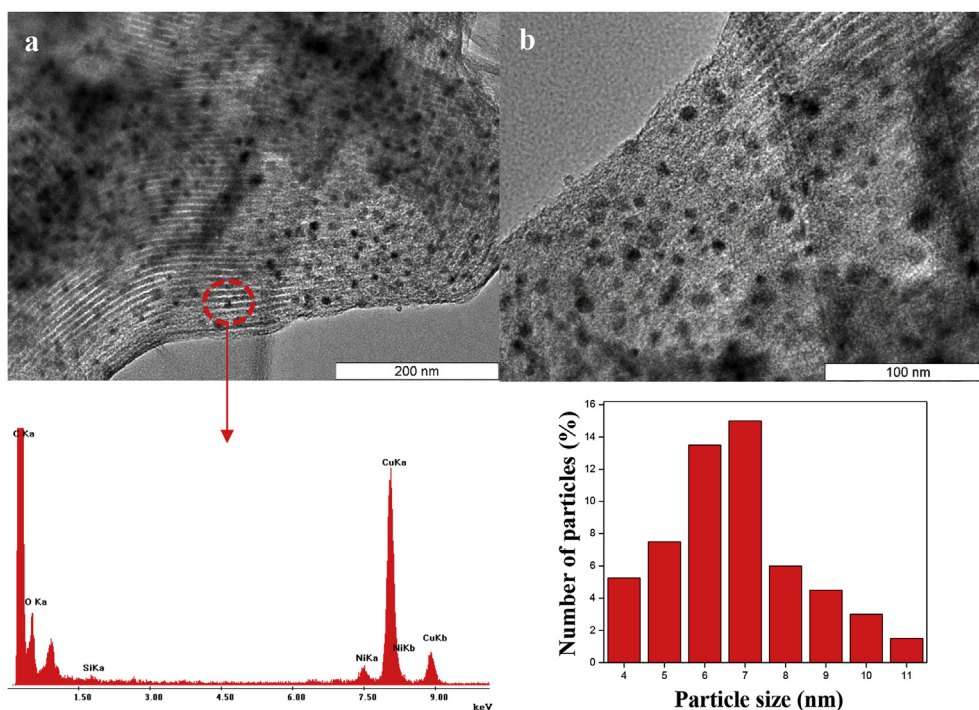

Fig. 4. Transmission electron microscopy images of (a–b) Ni/CMK-3 (2.5), EDS spectrum taken from the marked area and particle size distribution.
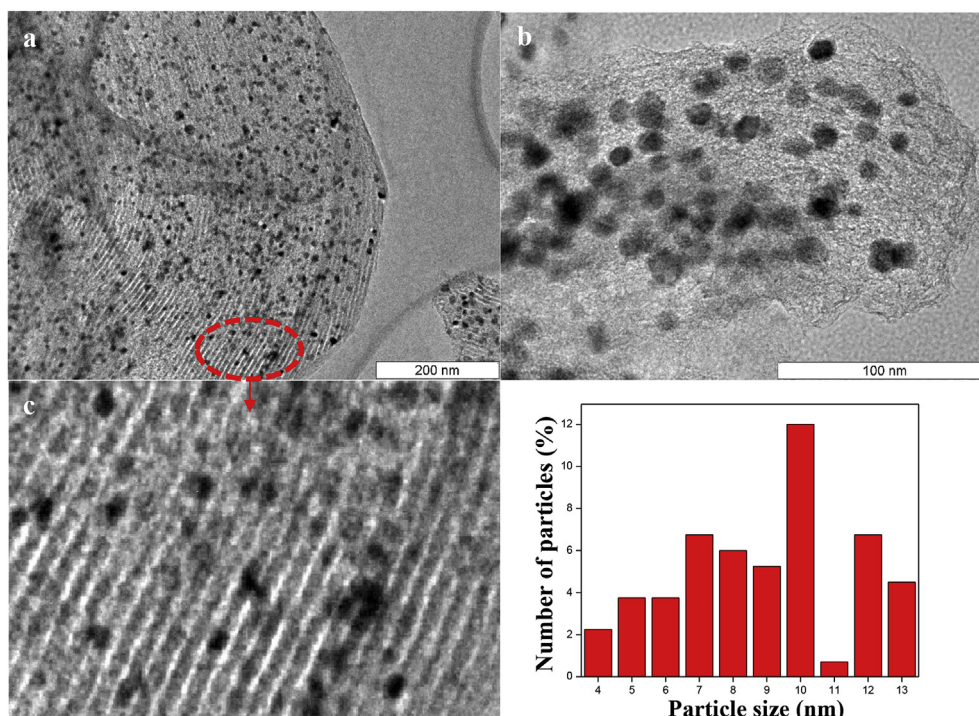
Fig. 5. Transmission electron microscopy images of (a-b-c) Ni/CMK-3 (10) and particle size distribution.
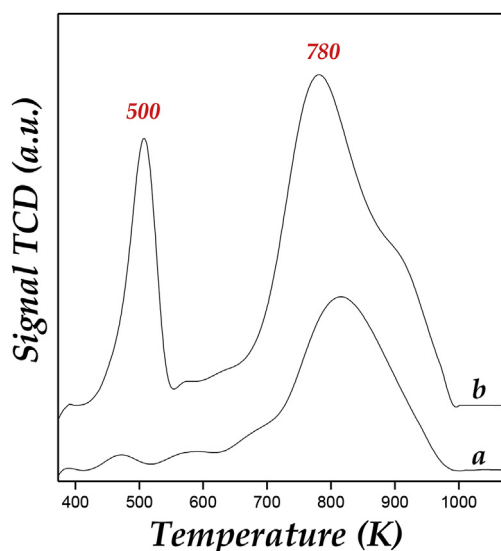

Fig. 6. TPR profiles of the (a) Ni/CMK-3 (2.5) and (b) Ni/CMK-3 (10) materials.

Fig. 7. XPS spectra of the Ni/CMK-3 samples (unreduced).

geometry the H_2 molecule was place close to the Ni atom in the Ni-C structure. The optimized geometry indicates that the H_2 molecule moves away from the Ni-C to (Fig. S5.c-d). Both geometries indicate that the Ni atom in the NiC system is not available to store H_2.

Fig. 10 shows how change the differential electronic density due to the C bonded on Ni/graphene. The later was calculated according of the following equation:

$$\Delta\eta = \eta_{graphs}/ \ NiC - (\eta_{graph}/Ni + \eta_C) \tag{1}$$

This figure shows that the carbon atom in NiC generates a depletion of density of charge of the Ni atoms. These could be the reason that the Ni atom does not interact with hydrogen molecule. Thus, when NiC it is formed, the Ni atoms loss the capacity of hydrogen storage as consequence of the electronic density transfer from the Ni atom to C atom in the metal-carbide structure.
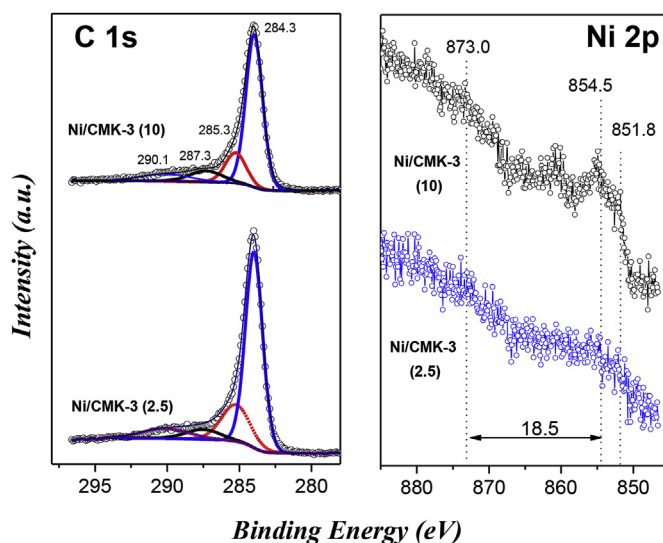
3.3. Hydrogen adsorption measurements

3.3.1. Low-pressure H_2 adsorption

The excess hydrogen uptakes measurements performed at 77 K and up to 10 bar are shown in Fig. 11. It is noteworthy that the adsorption–desorption process is completely reversible with negligible hysteresis. Also, it is interesting to compare the hydrogen adsorption isotherms of carbonaceous materials in logarithmic scale (Figure inset) to appreciate the differences in H_2 adsorption. These differences can be associated with the pore size and the adsorbate-adsorbent interactions.
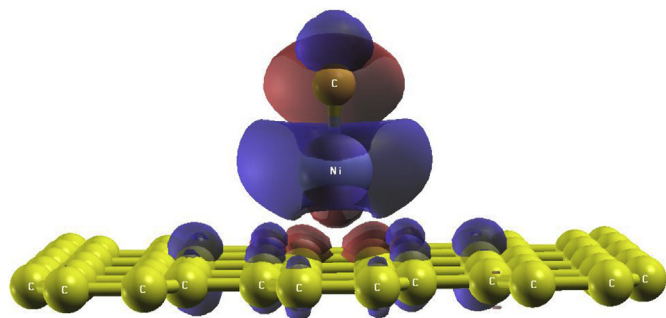
The pure CMK-3 and the Ni/CMK-3 (2.5) samples present similar H_2 adsorption capacity al low pressure (up to 1 bar). However, this behavior is modified at higher pressures, where the CMK-3 sample reaches the higher capacity of H_2 storage around 1.95 % wt. near 10 bar. Thus, the hydrogen adsorption capacity at 77 K decreases with the nickel
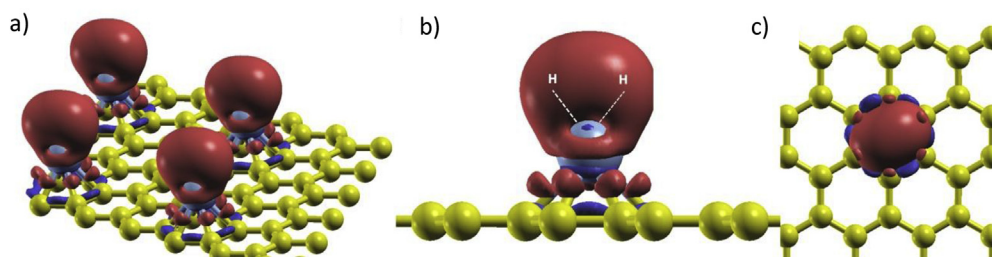
Fig. 8. Pseudo charge difference of H$_2$ adsorption on Ni/graphene compared with Ni, graphene and H atoms at the same positions at vacuum. a) H$_2$ on Ni/graphene, b) lateral view, and c) upper view. Red lobes indicate accumulation and blue lobes depletion. Isosurface value 0.001 eV/Å^3. (For interpretation of the references to color in this figure legend, the reader is referred to the Web version of this article.)
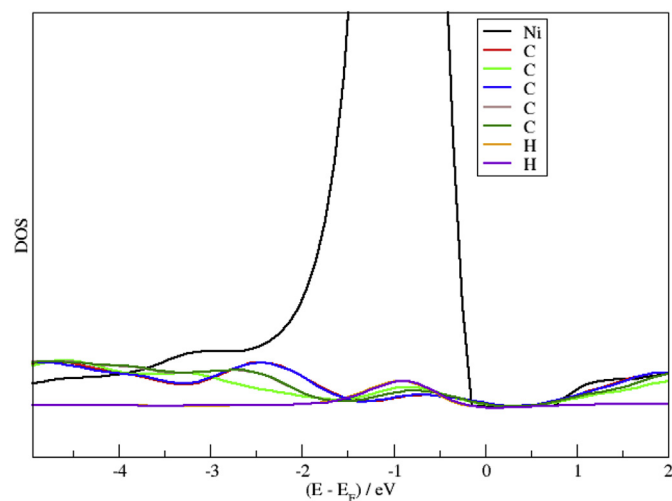
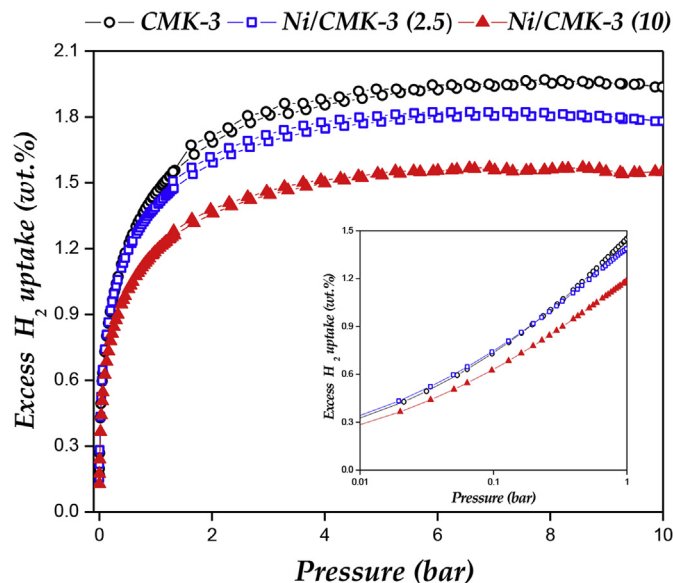Fig. 9. Projected density of states of the graphene/Ni/H$_2$ system. Carbon atoms shown in the plot are the linked to the Ni atom.

Fig. 11. H$_2$ adsorption-desorption isotherms of the synthesized samples, measured at 77 K. Inserted figure shows the amplified region for low pressures.

0.16 cm^3/g) presented the best results, which implies that for the carbon materials studied in this work, high specific surface areas are essential for hydrogen sorption at 77 K.

Fig. 10. Differential electronic density for NiC/graphene. Blue lobules indicate depletion of charge, red lobules accumulation of charge. Value of isosurface 0.005 e/Bohr^3. (For interpretation of the references to color in this figure legend, the reader is referred to the Web version of this article.)

incorporation in the mesoporous carbons frameworks, which decreases the pore volume accessible to hydrogen. Therefore, the metal incorporation, in its non-reduced form, into CMK-3 carbons diminishes H$_2$ adsorption at 77 K, which has already been observed by other authors [5,13,46]. This fact could be related with the presence of nickel carbide species on the support, which would not be favorable to the H$_2$ adsorption. Moreover, the behavior of these sites in the hydrogen adsorption was evidenced by the DFT calculations, where not improvement of H$_2$ interactions was observed for NiC/graphene and NiO/grapehen systems. Sigal et al. [45] have studied the latter system.

According to these results and taking into account that at liquid nitrogen temperature (77 K) the physisorption is a dominant mechanism, the nickel species formed in the support are not perhaps species responsible for the H$_2$ adsorption. Thus, the textural properties of the materials would be the determining factor in the H$_2$ storage capacity. In fact, CMK-3 sample (S_{BET}: 972 m^2/g, V$_T$: 0.99 cm^3/g and V$_{\mu P}$:

3.3.2. High pressure H$_2$ adsorption

In order to evaluate the metallic nickel influence to the H$_2$ storage capacity, reduction experiments were carried out for the samples, according to previous results [15]. The samples were treated under H$_2$ flow (215 mL/min) in pure H$_2$ at 723 K for 6 h with a ramp rate of 1 K/min.

The behavior of these materials changes dramatically with the reduction treatment. Hydrogen adsorption isotherms measured at 293 K and up to 35 bar are presented in Fig. 12. It should be further noted that the adsorption and desorption data are located practically at the same curves with a negligible hysteresis. The amount of hydrogen uptake increased significantly from 35 cm^3/g for CMK-3 to 55 cm^3/g for the reduced Ni/CMK-3 (2.5). Both CMK-3 and Ni/CMK-3 (2.5) materials hold ordered mesoporous structures and present similar textural properties confirmed by XRD and N$_2$ isotherms at 77 K, but a notable increase in hydrogen storage capacity was obtained in Ni/CMK-3 (2.5) sample. Thus, the metallic nickel presence could play an important role in the increase of hydrogen adsorption at 298 K. The sorption isotherm of Ni/CMK-3 (2.5) sample presents a steep increase in the H$_2$ adsorption, followed by a plateau at pressures close to 15 bar. This increase could be related to a synergistic effect between metallic nickel species presence highly dispersed in the mesoporous carbon and the carbon support.

On the other hand, the hydrogen storage capacity decreased with increasing nickel loading on the support (Ni/CMK-3 (10)), which could be attributed to an increase in the size of the nickel species on the
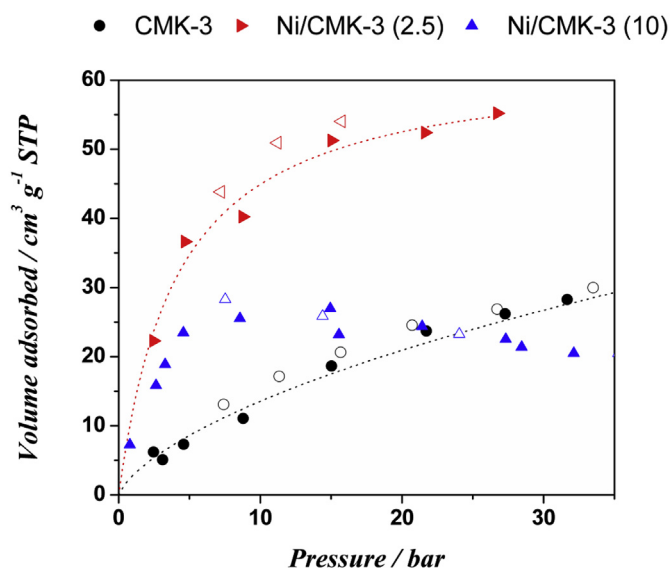
Fig. 12. H$_2$ adsorption (closed symbols) and desorption (open symbols) iso-therms of the Ni/CMK-3 materials and pure CMK-3 at 293 K up to 35 bar.

support. This fact could be due not only to a pore blocking, but also to a particle size effect. Figs. 4 and 5 showed that in Ni/CMK-3 (2.5) nickel nanoparticles are mainly 6–7 nm, whereas in Ni/CMK-3 (10) their particle sizes are larger. It is known that, hydrogen storage by spillover has been suggested as a mechanism to enhance the storage capacity of carbon nanostructures. This phenomenon consists of dissociative che-misorption of hydrogen on metal surface and subsequent diffuse of hydrogen atoms into the support [47,48]. Thus, a large surface area of the metal particle for the dissociative chemisorption of hydrogen and subsequent migration onto the carbon receptor is crucial to the metal activity. However, increasing nickel loading on the CMK-3 support, the nickel particle size was increased, which decrease the hydrogen storage capacity of these materials.

Therefore, a low metal loading allows highly stabilized-dispersion of Ni nanoparticles on the frameworks and it leads also to generating small Ni particle size, leading to an improvement in the hydrogen storage capacity of carbon materials. Thus, it can be concluded that to increase the hydrogen storage in this kind of materials, the control of the particle size and the degree of dispersion of Ni is fundamental, due to the im-portant role that Ni particle size plays in hydrogen storage. In addition, the CMK-3 has shown to be an adequate support for the stabilization of nickel nanoparticles for hydrogen storage at room temperature.

4. Conclusions

The Ni nano-particles were successfully dispersed over CMK-3 sample by a wet impregnation process, which play an important role in the hydrogen storage at the conditions under study. The nickel species detected on the support are in the NiC and NiO phases, according to XRD and XPS analyses. Thus, CMK-3 sample presented a high capacity of H$_2$ storage at 77 K, meanwhile, the samples modified with nickel loadings showed minor adsorption capacities. DFT calculations in-dicated the NiC on the support did not improve the H$_2$ adsorption ca-pacity, as consequence of the electronic density transfer from the Ni atom to C atom in the metal-carbide structure. However, the results showed an improvement in the hydrogen adsorption capacity at room temperature and high pressure, after reduction treatment. This improve due to presence of metallic nickel species, also is related to the high dispersion and the size of the nickel nanoparticles in the mesoporous carbon. These results highlight the importance of nickel nanoparticle size and their dispersion on the carbon support for improving hydrogen storage capacity.

Appendix A. Supplementary data

Supplementary data related to this article can be found at http://dx.doi.org/10.1016/j.micromeso.2018.06.057.

References

[1] J.H.N. van Vucht, F.A. Kuijpers, H.C.A.M. Bruning, Philips Res. Rep. 25 (1970) 133–140.
[2] K.T. Møllera, T.R. Jensena, E. Akibab, H. Lib, Prog. Nat. Sci.: Materials International 27 (2017) 34–40.
[3] S. Jun, S.H. Joo, R. Ryoo, M. Kruk, M. Jaroniec, Z. Liu, T. Ohsuna, O. Terasaki, J. Am. Chem. Soc. 122 (2000) 10712–10713.
[4] A.H. Lu, W.C. Li, W. Schmidt, F. Schüth, Microporous Mesoporous Mater. 80 (2005) 117–128.
[5] D. Giasafaki, A. Bourlinos, G. Charalambopoulou, A. Stubos, T.H. Steriotis, Microporous Mesoporous Mater. 154 (2012) 74–81.
[6] W. Curtis Conner, J.L. Falconer, Chem. Rev. 95 (1995) 759–788.
[7] R. Prins, Chem. Rev. 112 (2012) 2714–2738.
[8] T. Zhao, X. Ji, W. Jin, W. Yang, T. Li, Fullerenes, Nanotub. Carbon Nanostruct. 25–6 (2017) 355–358.
[9] G.J. Kubas, Acc. Chem. Res. 21 (1988) 120–128.
[10] B.-J. Kim, S.-J. Park, Int. J. Hydrog. Energy 36 (2011) 648–653.
[11] M. Anbia, S. Mandegarzad, J. Alloy. Comp. 532 (2012) 61–67.
[12] C.-C. Huang, Y.-H. Li, Y.-W. Wang, C.-H. Chen, Int. J. Hydrogen Energy 38 (2013) 3994–4002.
[13] J.M. Juárez, M.B. Gómez, O.A. Anunziata, Int. J. Energy Res. 39 (2015) 941–953.
[14] L. Wang, R.T. Yang, Energy Environ. Sci. 1 (2008) 268–279.
[15] P.M. Carraro, A.A. García Blanco, F.A. Soria, G. Lener, K. Sapag, G.A. Eimer, M.I. Oliva, Microporous Mesoporous Mater. 231 (2016) 31–39.
[16] D. Barrera, M. Dávila, V. Cornette, J.C.A. Oliveira, R. López, K. Sapag, Microporous Mesoporous Mater. 180 (2013) 71–78.
[17] P.M. Carraro, A.A. García Blanco, C. Chanquía, K. Sapag, M.I. Oliva, G.A. Eimer, Microporous Mesoporous Mater. 248 (2017) 62–71.
[18] F. Rouquerol, J. Rouquerol, K.S.W. Sing, P. Llewellyn, G. Maurin, Adsorption by Powders and Porous Solids: Principles, Methodology and Applications, Academic Press, San Diego, 2014.
[19] P. Giannozzi, et al., J. Phys. Condens. Matter 21 (2009) 1–9.
[20] M.C. Payne, M.P. Teter, C. Allan, T.A. Arias, J.D. Joannopoulos, Rev. Mod. Phys. 64 (1992) 1045–1097.
[21] H. Andrea Dal Corso, pbe-rrkjus.UPF, Ni.pbe-nd-rrkjus.UPF, C.pbe-d-rrkjus, http://www.quantum-espresso.org, (2014) online.
[22] G. Henkelman, B.P. Uberuaga, H.A. Jonsson, J. Chem. Phys. 113 (2000) 9901–9904.
[23] Z.Z. Lin, X. Chen, C. Yin, H. Tang, Y.C. Hu, X.J. Ning, Europhys. Lett. 96 (2011) 66005.
[24] M.C. Payne, et al., Rev. Mod. Phys. 64 (1992) 1045–1097.
[25] A. Kokalj, Comput. Mater. Sci. 28 (2003) 155–168.
[26] D.H. Everett, Manual of Symbols and Terminology for Physicochemical Quantities and Units-Appendix II. Definitions, Terminology and Symbols in Colloid and Surface Chemistry. Part I, IUPAC, 1971.
[27] P.I. Ravikovitch, A.V. Neimark, J. Phys. Chem. B 105 (2001) 6817–6823.
[28] P.M. Carraro, V. Elías, A.A. García Blanco, K. Sapag, S. Moreno, G.A. Eimer, M.I. Oliva, Microporous Mesoporous Mater. 191 (2014) 103–111.
[29] H. Zhang, H. Tao, Y. Jiang, Z. Jiao, M. Wu, B. Zhao, J. Power Sources 195 (2010) 2950–2955.
[30] H. Li, S. Zhu, H. Xi, R. Wang, Microporous Mesoporous Mater. 89 (2006) 196–203.
[31] V.C.H. Kroll, P. Delichure, C. Mirodatos, Kinet. Catal. 37 (5) (1996) 698–705.
[32] J. Matos, K. Díaz, V. García, T.C. Cordero, J.L. Brito, Catal. Lett. 109 (2006) 163–169.
[33] J. Kang, R. Han, J. Wang, L. Yang, G. Fan, F. Li, Chem. Eng. J. 275 (2015) 36–44.
[34] S. Nagakura, J. Phys. Soc. Jpn. 12 (1957) 428–294.
[35] Y. Cao, J. Cao, M. Zheng, J. Liu, G. Ji, J. Solid State Chem. 180 (2007) 792–798.
[36] K. Xia, Q. Gao, C. Wu, S. Song, M. Ruan, Carbon 45 (2007) 1989–1996.
[37] M.-Y. Cheng, B.-J. Hwang, J. Power Sources 195 (2010) 4977–4983.
[38] L. Samiee, F. Shoghi, A. Vinu, Appl. Surf. Sci. 265 (2013) 214–221.
[39] Y. Cao, J. Cao, M. Zheng, J. Liu, G. Ji, J. Solid State Chem. 180 (2007) 792–798.
[40] T.L. Barr, S. Seal, J. Vac. Sci. Technol., A 13 (1995) 1239–1246.
[41] P. Niebzydowska, R. Janus, P. Kustrowski, S. Jarczewski, A. Wach, A.M. Silvestre-Albero, F. Rodríguez-Reinoso, Carbon 64 (2013) 252–261.

[42] C.D. Wagner, W.M. Riggs, L.E. Davis, J.F. Moulder, G.E. Muilenberg, Handbook of X-ray Photoelectron Spectroscopy, Perkin-Elmer Corporation, Eden Prairie, 1979.
[43] I. Czekaj, F. Loviat, F. Raimondi, J. Wambach, S. Biollaz, A. Wokaun, Appl. Catal. A-Gen 329 (2007) 68–78.
[44] V. Barone, M. Casarin, D. Forrer, M. Pavone, M. Sambi, A. Vittadini, J. Comput. Chem. 30 (2009) 934–939.
[45] A. Sigal, M.I. Rojas, E.P.M. Leiva, Int. J. Hydrogen Energy 36 (2011) 3537–3546.
[46] A. Yadav, M. Faisal, A. Subramaniam, N. Verma, Int. J. Hydrogen Energy 42 (2017) 6104–6117.
[47] R. Prins, Chem. Rev. 112 (5) (2012) 2714–2738.
[48] L. Wang, R.T. Yang, Catal. Rev. Sci. Eng. 52 (4) (2010) 411–461.